

Article

Open Access

J. Mex. Chem. Soc. **2026**, 70(1):e2475

Received April 14th, 2025

Accepted September 24th, 2025

<http://dx.doi.org/10.29356/jmcs.v70i1.2475>

e-location ID: 2475

Keywords:

ZnO-MgO Nanocomposites, microwave synthesis, antimicrobial activity

Palabras clave:

Nanocompuestos de ZnO-MgO, síntesis por microondas, actividad antimicrobiana

*Corresponding author:

Pérez Larios Alejandro

email: alarios@cualtos.udg.mx

Antimicrobial Effect on Pathogenic Microorganisms and Physicochemical Characterization of Zn-MgO Nanocomposites

Miramontes-Escobar Herenia Adilene², Ruvalcaba-Díaz Betsy Krisel¹, Sánchez-Burgos Jorge Alberto¹, Suresh Ghotekar³, Mamoun Fellah⁴, Pérez Larios Alejandro^{2*}

¹National Technological Institute of Mexico/ Technological Institute of Tepic, Food Research Laboratory, Instituto Tecnológico Avenue No 2595, Lagos del Country CP 63175, Tepic, Nayarit, Mexico.

²Nanocatalysis Research Laboratory, Department of Engineering, Centro Universitario de los Altos, University of Guadalajara, Tepatitlán de Morelos, Mexico.

³Centre for Herbal Pharmacology and Environmental Sustainability, Chettinad Hospital and Research Institute, Chettinad Academy of Research and Education, Kelambakkam 603103, Tamil Nadu, India.

⁴Mechanical Engineering Department, ABBES Laghrour University, P.O 1252, 40004 Khenchela, Algeria.

Abstract. Zn-MgO nanocomposites have attracted interest due to their antimicrobial potential against pathogens. The antimicrobial activity of ZnO/MgO mixed oxides with different ratios (1 %, 3 %, 5 % w/w) was evaluated against *Escherichia coli*, *Enterococcus faecalis*, *Staphylococcus aureus*, *Salmonella paratyphi A*, and *Listeria monocytogenes*. The nanomaterials were synthesized using the microwave method and characterized by FT-IR, XRD, and SEM, confirming the presence of Zn-O and Mg-O bonds, particle sizes ranging from 20 to 42 nm, and cubic/semiglobular morphologies. The results revealed that the addition of MgO influences the particle size and the MgO ratio used, with 1 % ZM being the most effective treatment. This study contributes to the development of new antimicrobial agents to combat the growing bacterial resistance.

Resumen. Los nanocompuestos de Zn-MgO han despertado interés por su potencial antimicrobiano contra patógenos. Se evaluó la actividad antimicrobiana de óxidos mixtos de ZnO/MgO con diferentes relaciones (1 %, 3 %, 5 % w/w) sobre *Escherichia coli*, *Enterococcus faecalis*, *Staphylococcus aureus*, *Salmonella paratyphi A* y *Listeria monocytogenes*. Los nanomateriales fueron sintetizados mediante el método de microondas y caracterizados por FT-IR, DRX y SEM, confirmando la presencia de enlaces Zn-O y Mg-O, tamaños de partícula entre 20-42 nm y morfologías cúbicas/semiglobulares. Los resultados revelaron que la adición de MgO influye en el tamaño de partícula y la relación de MgO utilizada, siendo el mejor tratamiento ZM 1 %. Este estudio contribuye al desarrollo de nuevos agentes antimicrobianos para combatir la creciente resistencia bacteriana.

Introduction

Research on Zn-MgO nanocomposites has generated significant interest due to their potential application as antimicrobial agents against pathogenic microorganisms, particularly in the context of the global health crisis posed by antimicrobial resistance (AMR). According to the World Health Organization, antimicrobial-resistant infections account for nearly 5 million deaths annually, highlighting the urgent need for novel alternatives to conventional antibiotics. Traditional strategies are increasingly limited by reduced efficacy, the emergence of multidrug-resistant strains, and the ability of microorganisms to form biofilms that protect them from conventional treatments. ZnO-MgO nanocomposites have demonstrated antimicrobial activity against gram-positive bacteria, such as *Staphylococcus aureus*, and gram-negative bacteria, including *Escherichia coli* and *Pseudomonas aeruginosa* [1-3], as well as against pathogenic fungi such as *Candida albicans* [4-5]. Their antimicrobial mechanism is multifactorial and primarily involves the release of Zn^{2+} and Mg^{2+} ions coupled with the generation of reactive oxygen species (ROS). These ROS, including superoxide anion ($\text{O}_2^{\bullet-}$), hydroxyl radicals ($\bullet\text{OH}$), and hydrogen peroxide (H_2O_2), interact with microbial targets in several ways: (i) peroxidation of membrane lipids, leading to increased permeability and cell lysis; (ii) oxidation of proteins and enzymes, causing metabolic dysfunction; and (iii) damage to nucleic acids, resulting in impaired replication and cell death. This multi-target oxidative stress response provides a significant advantage over conventional antibiotics, as it reduces the likelihood of microorganisms developing resistance [6]. Moreover, ZnO-MgO nanocomposites have shown the ability to inhibit biofilm formation, an essential factor in combating persistent and recurrent infections [7,8]. Biofilms act as physical and biochemical barriers against antimicrobial agents, contributing to the survival of pathogens in clinical and industrial settings. By disrupting biofilm integrity, these ZnO-MgO nanocomposites represent a novel strategy to overcome one of the main challenges in infection control.

Recent advances in synthesis methods, such as plant-assisted and ultrasound-mediated synthesis, have improved the biocompatibility, stability, and sustainability of ZnO-MgO nanocomposites [4,7]. These techniques not only reduce the environmental footprint but also provide materials with tailored physicochemical properties that enhance their antimicrobial efficacy. Nonetheless, challenges remain in terms of large-scale application, reproducibility of synthesis, and integration into biomedical systems, underscoring the importance of further experimental evaluation to augment their antimicrobial properties and expand their therapeutic applications, particularly in the context of treating infections that have developed resistance to antibiotics [6,9].

In this context, the present study aims to evaluate the antimicrobial effect of ZnO and MgO mixed oxides at different molar ratios against clinically relevant pathogenic bacteria, including *Escherichia coli*, *Enterococcus faecalis*, *Staphylococcus aureus*, *Salmonella Paratyphi A*, and *Listeria monocytogenes*. This work aims to provide further insight into the antimicrobial potential of ZnO-MgO nanocomposites and perspectives for their application as innovative alternatives to address the pressing issue of antimicrobial resistance.

Experimental

The reagents utilized in the development of the nanomaterials were procured from Sigma-Aldrich. The microwave synthesis was carried out using a Monowave 50 apparatus (synthesis reactor Monowave 50, Anton Paar, Graz, Austria). The FT-IR characterization was performed using an FT-IR spectrophotometer (Nicolet iS5, ThermoFisher Scientific, Tokyo, Japan) with the aid of specular reflectance. X-ray diffraction analysis (XRD) was performed using an Empyrean instrument (Malvern Panalytical, Almelo, The Netherlands), while scanning electron microscopy (SEM) was conducted on a Tescan Model MIRA 3LMU (Tescan, UK). Transmission electron microscopy was carried out using a Jeol Model JEM ARM200F (Boston, MA, USA).

Synthesis and characterization

Experimental design

A completely randomized one-factor experimental design model was utilized, wherein the independent variable was the concentration of MgO in the ZnO-MgO system (1 %, 3 %, and 5 % by weight). For each concentration level, three independent replicates ($n = 9$) were prepared, and the synthesis parameters were strictly controlled to ensure consistency. These parameters included temperature (150 °C), reaction time (3 min), and calcination protocol (500 °C/5 h). The dependent variables evaluated included particle size, X-ray diffraction (XRD), Fourier transform infrared (FTIR), and antimicrobial activity. Statistical analysis was performed by one-factor ANOVA, and the assumptions of normality (Shapiro-Wilk test) and homogeneity of variances (Levene's test) were verified. Post-hoc comparisons were performed by Tukey HSD using Statistica Version 12 (Statsoft, 2012), establishing a significance level $\alpha=0.05$.

ZnO-MgO synthesis

The synthesis was carried out in accordance with the methodology outlined by [10]. The following reagents were utilized: dihydrated zinc acetate ($C_4H_6O_4Zn \cdot 2H_2O$) as the precursor, magnesium nitrate hexahydrate ($Mg(NO_3)_2 \cdot 6H_2O$) as the dopant, and 1% of each component. 3 % and 5 % by weight in a solution of ethyl alcohol (CH_3CH_2OH) and distilled water (H_2O). Then, a Monowave 50 microwave (synthesis reactor Monowave 50, Anton Paar, Graz, Austria) was used at 150 °C for 3 min. After the synthesis, the samples were subjected to a drying process for a duration of 24 hours, after which they were calcined at a temperature of 500 °C for a duration of 5 hours. This step was undertaken to ensure the complete removal of any residual substances resulting from the synthesis. The synthesis scheme utilized is depicted in Fig. 1.

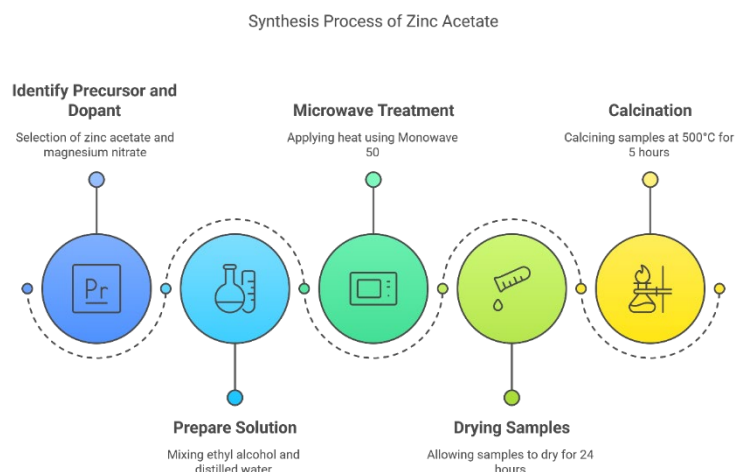


Fig. 1. Flow chart for synthesis by microwave method.

The nanocomposites were labeled as ZM X%, where “ZM” refers to the ZnO–MgO system and “X” indicates the MgO concentration incorporated into the composite (1 %, 3 %, and 5 % by weight). Thus, ZM 1%, ZM 3 %, and ZM 5 % correspond to ZnO–MgO nanomaterials containing 1, 3, and 5 wt% of MgO, respectively.

Structural and morphological characterization

FT-IR spectroscopy

The identification of functional groups and prevalence of bonds of the synthesized nanomaterial was obtained using the FT-IR spectrometer (Nicolet iS5, ThermoFisher Scientific, Tokyo, Japan) with the aid of specular reflectance (for its non-destructive analysis). The spectrum was recorded at room temperature (25 °C), with 24 scans and 4 cm⁻¹ resolution.

X-ray diffraction

The analysis was performed at a voltage of 40 kV and a current of 30 mA using Empyrean diffraction equipment (Malvern Panalytical, Almelo, The Netherlands). Diffraction intensity as a function of diffraction angle (2θ) was measured between 4° and 70°, using a step of 0.03 ° and a counting time of 0.3 s per step, to determine the particle size measurement, and in this way provided information to identify and quantify the components present in the nanomaterials. From these measurements, the particle size was determined by means of the Debye-Scherrer formula (Equation 1):

$$D = \frac{K\lambda}{\beta \cos \theta} \quad (1)$$

Where D is the crystal size and λ is the wavelength of X-ray radiation (λ = 0.15406 nm for CuKα), K is the shape factor (commonly taken as 0.9, see Equation 2), and β is the full width at half maximum (FWHM) of the diffraction peak, of the diffraction peak expressed in radians (calculated from Equation 3) and θ is the Bragg angle.

For practical purposes, Equation (1) can be written as:

$$D = \frac{K\lambda}{\beta \cos \theta} = \frac{(0.9)(0.15406)}{\beta \cos \theta} \quad (2)$$

The line broadening parameter β in radians is obtained from the full width at half maximum (FWHM, measured in degrees) using the following relation:

$$\beta = \frac{\pi}{180} \times \text{FWHM} \quad (3)$$

Scanning electron microscopy (SEM)

The morphology was analyzed by scanning electron microscopy [11] (Tescan, MIRA 3LMU, UK) at 20 kV to a total of 5 nanomaterials. The samples were previously placed on a carbon tape and coated by sputtering with a conductive material (Gold) for 20 s (0.1 mL/s), with which magnifications of 50,000–100,000 (up to 4 nm) can be realized.

Transmission electron microscopy (TEM)

High-resolution images were obtained using a transmission electron microscope (Jeol, JEM ARM200F, Boston, MA, USA) operated at 200 kV. The images were then subjected to analysis using specialized software (Gatan Micrograph v. 3.7.0, Gatan Inc., Pleasanton, CA, USA).

Antimicrobial Activity

Antimicrobial activity was determined by the Kirby-Bauer method with adaptations for sensidisks as described by [10], this procedure yielded a disc-plate antibiogram. The methodology was performed according to protocols M07-A9: Methods for Dilution Antimicrobial Susceptibility Tests for Bacteria That Grow Aerobically; Approved Standard, and M26-A: Methods for Dilution Antimicrobial Susceptibility Tests for Bacteria That Grow Aerobically of the Clinical and Laboratory Standards Institute (CLSI). The medium utilized for the tests was recommended by CLSI and the Committee on Antimicrobial Susceptibility Testing (EUCAST); namely, Mueller-Hinton Broth. Prior to this study, the following strains were cultivated on Mueller-Hinton agar plates: *Escherichia coli* (ATCC8939), *Enterococcus faecalis* (ATCC19433), *Staphylococcus aureus* (ATCC33862), *Salmonella paratyphi A* (ATCC9150), and *Listeria monocytogenes* (ATCC15313). The preparation of the medium was performed according to the manufacturer's specifications (BD bioxon). The antimicrobial activity of ZnO, MgO, ZM 1 %, ZM 3 %, and ZM 5 % were evaluated using positive (ampicillin 50 µg/mL) and negative (water) controls. Once the strains were under optimal growth conditions, an aliquot was taken from each of the strains to be evaluated and inoculated in Mueller-Hinton broth. The inoculated broth was then incubated for 24 hours until reaching a concentration of 2×10^6 cells/mL. Once this concentration of cells was reached, sensidiscs impregnated with the nanomaterials (ZnO-Mg) as well as the positive (ampicillin, 50 mg/mL) and negative (water) controls were placed on plates with Mueller-Hinton agar, the experiment was performed with 3 replicates with 3 replicates. Subsequently, the plates were incubated at 38 °C for 24 h. After the incubation time, the inhibition halo was measured using a digital vernier and the results were expressed as the mean \pm standard deviation [12].

The potential antimicrobial effect was interpreted using the following criteria: sensitive (S, >17 mm), intermediate (I, 14-16 mm), or resistant (R, <13 mm) according to the categories established by the National Committee for Clinical Laboratory Standards (NCCLS).

Statistical analysis

Data analysis was performed using STATISTICA software (Stat Soft inc 1984-2014. Tulsa, OK, USA) version 12. Results were expressed as mean \pm standard deviation. A principal component analysis was performed on the data obtained, to determine the effect of variability according to the microorganism evaluated, particle size and treatments.

Results and discussion

Structural and morphological characterization

FT-IR spectroscopy

The characteristic vibrations of the functional groups and their possible interactions were analyzed by Fourier transform infrared spectroscopy (Fig. 2). In Fig. 2(A) (ZnO), bands were detected in the 550–650 cm^{-1} region, attributed to the Zn–O stretching vibrations, in agreement with the literature [13]. In Fig. 2(B) (MgO), a characteristic band at $\sim 667 \text{ cm}^{-1}$ was observed, corresponding to the Mg–O stretching mode [14]. In the spectra of the nanocomposites (Fig. 2(C–E): ZM 1 %, ZM 3 % and ZM 5 %), the characteristic signals of both Zn–O and Mg–O bonds (550, 650 and 667 cm^{-1}) were present regardless of the MgO concentration. Additionally, a weak band at $\sim 2329 \text{ cm}^{-1}$ was observed in all samples, which can be associated with adsorbed CO_2 (O=C=O vibrational mode), as reported in ZnO thin films prepared by the sol–gel dip-coating method [15]. The intensity of this band decreased progressively from ZM 1 % (Fig. 2(C)) to ZM 5% (Fig. 2(E)), suggesting that higher MgO content reduces CO_2 adsorption on the nanocomposite surface.

Broad signals in the 1500–1700 cm^{-1} region were also observed in the spectra of ZnO and the nanocomposites (Fig. 2(A), 2(C–E)). These bands are more reasonably attributed to surface adsorbed carbonate species or residual organics from synthesis, since the ZnO structure only contains Zn–O bonds. A contribution near 1600 cm^{-1} may also arise from molecular water adsorbed on the surface of the nanomaterials; however, in the absence of a broad O–H stretching band at 3000–3600 cm^{-1} , this attribution should be considered tentative [16]. Overall, the FT-IR analysis confirms the coexistence of Zn–O and Mg–O vibrations in the nanocomposites, together with minor contributions from adsorbed CO_2 and carbonate groups, which tend to decrease as the MgO concentration increases.

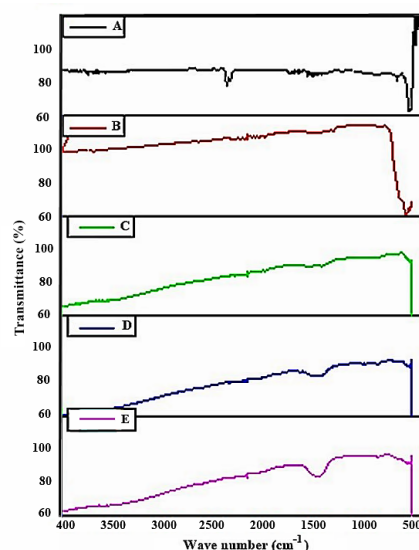


Fig. 2. FT-IR spectra of nanomaterials of (A) ZnO, (B) MgO, (C) ZM 1 %, (D) ZM 3 %, (E) ZM 5 %.

X-ray diffraction

X-ray diffraction (XRD) was employed to characterize the crystalline structure and estimate the particle size of ZnO, MgO, and their nanocomposites (ZM 1 %, ZM 3 %, ZM 5 %). Fig. 3 displays the diffraction patterns of the pure oxides and nanocomposites. The ZnO (3(A)) sample exhibited characteristic diffraction peaks at $2\theta = 31.60^\circ$ (100), 34.20° (002), 36.10° (101), 47.50° (102), 56.40° (110), 62.60° (103), and 68.80° (112), which match the JCPDS Card No. 00-001-1136. The MgO (3(B)) pattern showed peaks at 36.80° (111), 42.60° (200), 62.50° (220), 74.50° (311), and 78.40° (222), consistent with JCPDS Card No. 75-1525.

The diffraction patterns of the nanocomposites confirmed the presence of both ZnO and MgO crystalline phases (3(C), 3(D), and 3(E)), with the characteristic peaks of both materials visible. Although literature reports a decrease in the ZnO peak intensity with increasing MgO concentration, attributed to possible substitution of Zn^{2+} by smaller Mg^{2+} ions (ionic radii: 0.60 \AA vs. 0.57 \AA), such a trend is not distinctly observable in the present XRD data, possibly due to overlapping peaks and the resolution of the measurement.

Regarding particle size, calculated values were approximately 20 nm for ZnO, 42 nm for MgO, and between 23–26 nm for the nanocomposites. This aligns with previous reports where incorporation of Mg^{2+} ions is suggested to inhibit ZnO crystal growth, thereby affecting particle size variations [17-19].

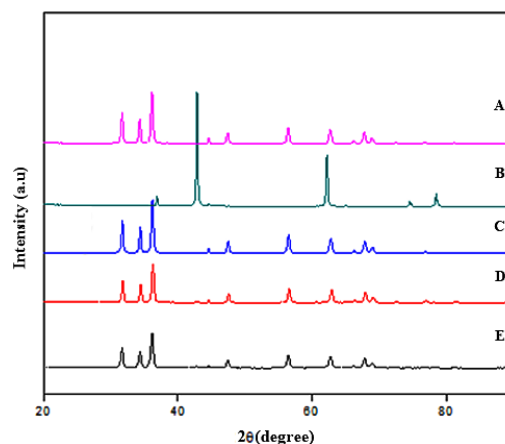


Fig. 3. X-ray diffraction of (A) ZnO, (B) MgO, (C) ZM 1 %, (D) ZM 3 %, (E) ZM 5 % nanomaterials.

Scanning electron microscopy (SEM)

The SEM micrographs presented in Fig. 4 show distinct morphologies for ZnO, MgO, and their nanocomposites at different dopant concentrations. 4(A) (ZnO) reveals nanoparticles predominantly agglomerated with relatively uniform shape, featuring facets that suggest cubic or semi-globular geometries, consistent with previous reports of microwave-synthesized ZnO nanoparticles [20]. 4(B) (MgO) shows larger aggregates with well-defined, smooth surfaces composed of nanoflake-like structures, confirming the expected morphology reported in the literature [21]. 4(C)-4(E) corresponds to the ZnO-MgO nanocomposites with increasing MgO content (1 %, 3 %, and 5 %). These SEM images demonstrate the preservation of characteristic morphologies from each oxide phase, with agglomerated particles showing a mixture of cubic and flake-like shapes. Notably, the nanoflakes appear to elongate progressively as the MgO concentration increases, suggesting that dopant level influences the growth and final morphology of the nanoflakes within the composite. This could be attributed to modified nucleation and growth mechanisms induced by the dopant during synthesis. Such morphological changes align with earlier studies that report dopant-induced variations in nanostructure shapes [22].

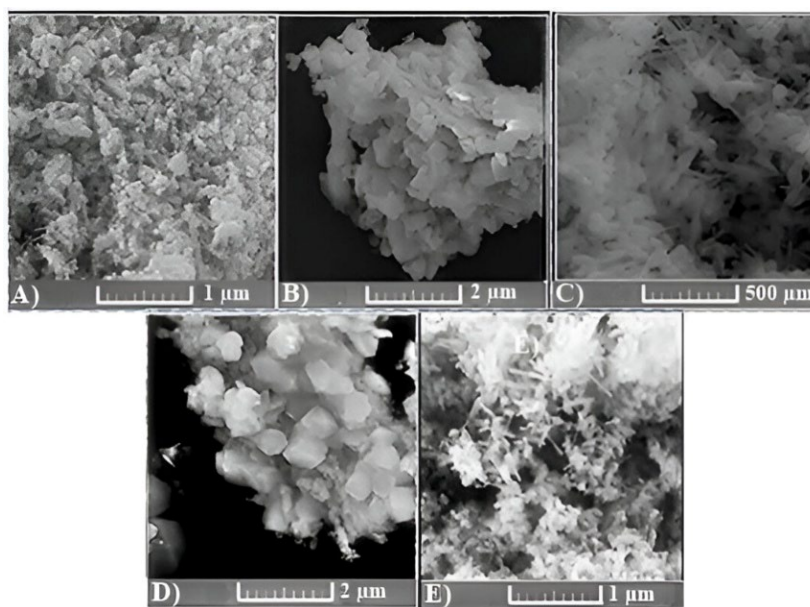


Fig. 4. SEM micrographies of (A) ZnO, (B) MgO, (C) ZM 1 %, (D) ZM 3 %, (E) ZM 5 %.

Transmission electron microscopy (TEM)

As illustrated in Fig. 5, the TEM images of the analyzed materials reveal the formation of tubular, elongated materials, and in some cases, spherical structures with sizes ranging from 20 to 49 nm. These calculations were performed using ImageJ software (Public Domain, BSD-2). The particles depicted in Fig. 5(A) and 5(B) were identified as ZnO and MgO, respectively. The former was predominantly composed of spherical structures, while the latter was primarily composed of elongated rods. The absence of discernible mixtures or contamination is indicated by the translucent interiors of the particles. In contrast, the microscopies of the ZM 1 %, ZM 3 %, and ZM 5 % nanocomposites (Fig. 5(C), 5(D), and 5(E), respectively) reveal the integration of the salts within the particles. The opacity of the particles' interiors suggests that they have undergone correct structuring, thereby validating the experimental methodology.

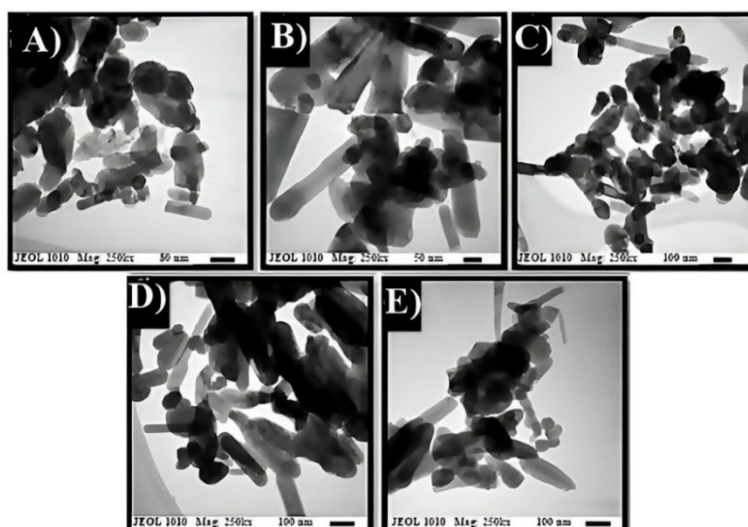


Fig. 5. TEM microscopy, (A) ZnO, (B) MgO, (C) ZM 1 %, (D) ZM 3 %, (E) ZM 5 %.

As illustrated in Fig. 6(c) and 6(e), the histograms obtained exhibited shapes analogous to those of normal distribution curves, suggesting a higher degree of homogeneity in the particle size. Fig. 6 presents the histograms of the particle size values that are consistent with those obtained by Scherrer's Equation (Equation 3), which was utilized in XRD. This equation yielded particle sizes of 20, 48, 24, 24, 26, and 23 nm for the treatments ZnO, MgO, ZM 1 %, ZM 3 %, and ZM 5 %, respectively. It was observed that there were no significant differences attributed to the amounts of dopant (MgO) used ($p > 0.05$). This observation suggests a correlation between the size of NPs in materials with dopant and the size of ZnO, given the prevalence of ZnO in the composition of these materials. According to Kumar et al., (2013) [23] the particle sizes reported for pure MgO nanoparticles were found to range from 28 to 64 nm. These values are consistent with the material's hygroscopic nature and the properties obtained. Additionally, the size of ZnO synthesized by the coprecipitation method, which was shown to be 20 nm as reported by Sankara Reddy et al., (2013) [24], is consistent with the observed sizes (Table 1). The subsequent analysis employing the Shapiro-Wilk normality test revealed the normalcy of ZnO, MgO, ZM 1%, and ZM 5% nanoparticle sizes. Conversely, ZM 3% exhibited non-normality ($P=0.00220$).

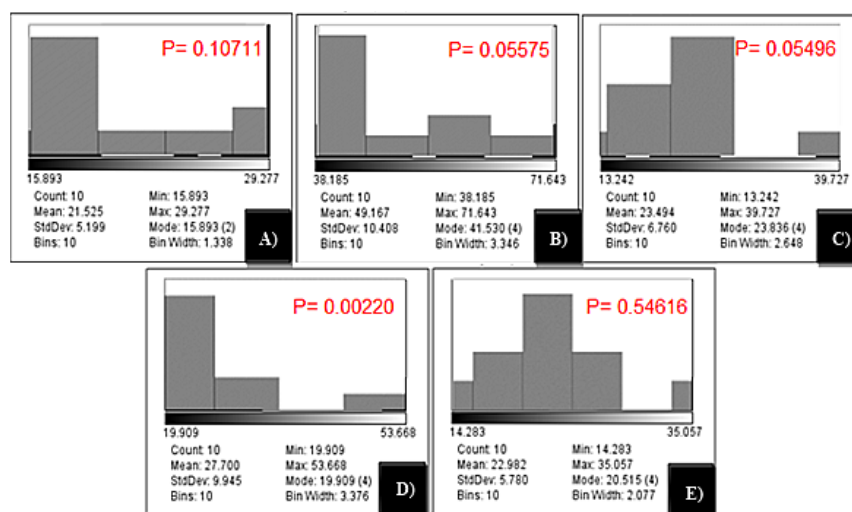


Fig. 6. Histograms of particle size distribution of the synthesized materials (A) ZnO, (B) MgO, (C) ZM 1 %, (D) ZM 3 %, (E) ZM 5 %.

Table 1. Average particle size of nanomaterials.

Material	Average particle size (nm)
ZnO	21 ± 5 a
MgO	49 ± 10 b
ZM 1 %	24 ± 6 a
ZM 3 %	27 ± 9 a
ZM 5 %	22 ± 5 a

*Different letters indicate significant differences. ZM 1 %: ZnO-MgO 1 %, ZM 3 %: ZnO-MgO 3 %, ZM 5 %: ZnO-MgO 5 %

Antimicrobial activity

The antimicrobial activity of the nanocomposites was evaluated using an antibiogram, the results of which are presented in Table 2. Table 3 shows the inhibition diameters obtained for ZnO and the different concentrations of ZnO-MgO (ZM 1 %, ZM 3 %, ZM 5 %), together with the positive and negative controls, against the pathogenic strains tested. The results demonstrated statistically significant differences ($p < 0.05$) between the treatments and the positive control. The ZnO-MgO mixed oxides (ZM 1 %, ZM 3 %, and ZM 5 %) exhibited antibacterial activity against both Gram-positive and Gram-negative bacteria, though the efficacy of this activity differed according to the type of microorganism. In general, the ZnO-MgO combination exhibited higher antimicrobial activity compared to ZnO alone. The ZM 1 % nanocomposite exhibited the most pronounced inhibition halos against *S. paratyphi* (31 %), *E. faecalis* (41 %), *E. coli* (38 %), and *L. monocytogenes* (10 %) when compared to the positive control, while the ZM 3 % nanocomposite demonstrated a more significant halo against *S. aureus*. This behavior suggests that higher concentrations of ZnO-MgO do not necessarily increase antimicrobial activity. This is probably due to the aggregation of the nanoparticles at high concentrations, which reduces their active surface area and consequently the release of Zn^{2+} and Mg^{2+} ions, fundamental for their antimicrobial activity [1]. ZnO-doped MG mixed oxides have been shown to generate reactive oxygen species such as H_2O_2 and O_2 , which can destabilize the cellular structures of bacteria, including peptidoglycan [25], other authors report that the use of ZnO nanoparticles in polymeric films also present the same antimicrobial effect through the generation of reactive oxygen species, damaging the cell wall and DNA [26].

Table 2. Antibiogram with ZnO sensidisks, ZM 1 %, ZM 3 %, ZM 5 %.


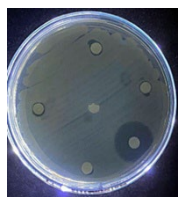

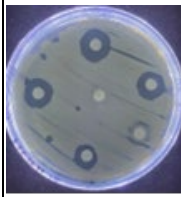
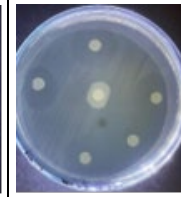
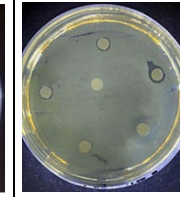
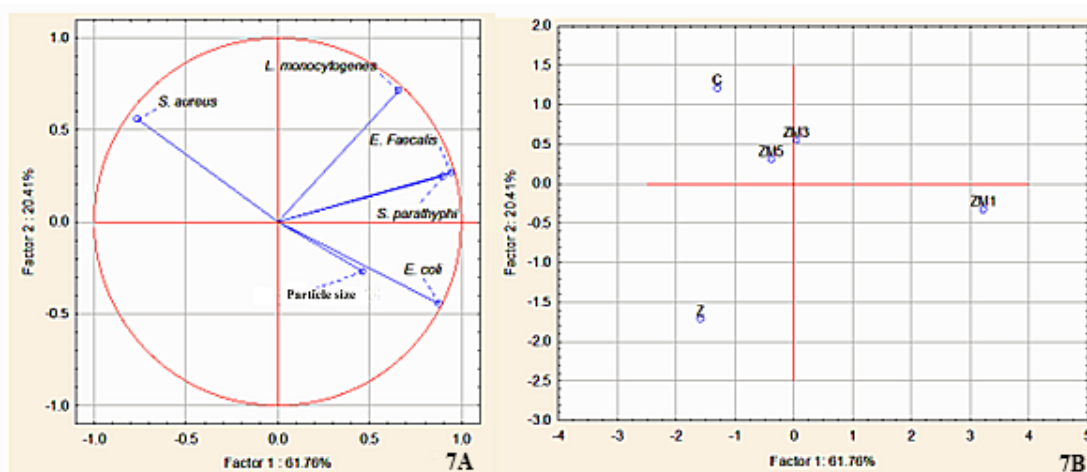
Material	Strains				
	<i>S. paratyphi</i> (ATCC 9150)	<i>E. Faecalis</i> (ATCC 19433)	<i>S. Aureus</i> (ATCC 33862)	<i>L. Monocytogenes</i> (ATCC 15313)	<i>E. coli</i> (ATCC 8939)
					

Table 3. Antimicrobial activity with inhibition halo values (mm) of ZnO, ZM 1 %, ZM 3 %, ZM 5 %.

Material	<i>S. paratyphi</i>	<i>E. Faecalis</i>	<i>S. aureus</i>	<i>L. monocytogenes</i>	<i>E. coli</i>
Ampicillin (C+)	16 ± 0.5 ^{ab}	17 ± 0.5 ^{ab}	19 ± 1 ^a	20 ± 1 ^a	13 ± 1.15 ^a
ZnO	13 ± 3.05 ^a	13 ± 2.08 ^a	15 ± 2.5 ^{ab}	15 ± 0.5 ^b	15 ± 2.3 ^a
ZM 1%	21 ± 1.73 ^b	24 ± 1.73 ^b	10 ± 0.5 ^b	22 ± 1.15 ^a	18 ± 0.5 ^a
ZM 3%	15 ± 3.055 ^a	18 ± 6.4 ^{ab}	19 ± 4.5 ^a	22 ± 2.08 ^a	15 ± 2.6 ^a
ZM 5%	17 ± 1.15 ^{ab}	16 ± 2.6 ^{ab}	17 ± 1.15 ^a	20 ± 1.15 ^a	14 ± 0 ^a

Values are the mean of triplicate determinations plus standard deviation. Different letters denote significant differences. One-way ANOVA/Tukey test was used ($p < 0.05$).

Principal Component Analysis (PCA) was performed to determine which mixed oxide exhibited the highest activity as a function of particle size and mixed oxide composition from the particle size data and antimicrobial assay results with the different strains evaluated (Fig. 7). Components A (7A) and B (7B) explained 82.2 % of the variability presented in the treatments, with Factor 1 accounting for 61.76 % of the variability and Factor 2 accounting for 20.41 %. As illustrated in Fig. 7(A), cases demonstrating a propensity for positive variation include antimicrobial activity against *E. coli*, *S. paratyphi*, and particle size. Regarding Factor 2, the cases demonstrating a positive trend are *S. aureus*, while *L. monocytogenes* exhibited a positive trend for both cases and *E. faecalis* exhibited a trend analogous to that of *S. paratyphi*. Treatments (Fig. 7(B)) demonstrate that the positive control (ampicillin) exhibits a similar positive trend in Factor 2 to that of *S. aureus*. In contrast, the treatments ZM 5 % and ZM 3 % do not align with the trend observed for the other treatments or cases. However, the effect of these treatments can be considered low (less than 1). Notably, ZM 1 % displays a positive trend in Factor 1, which is analogous to the trend exhibited by the cases of *E. coli* and particle size. This finding suggests that the ZM 3 % and ZM 5 % treatments may exert a comparable antimicrobial effect, as evidenced by the outcomes presented in Table 3.

**Fig. 7.** PCA diagram of: (A) Cases; (B) Treatments.

Conclusions

An antimicrobial effect of the mixed oxides (ZnO-MgO) was presented against the strains evaluated, showing their effectiveness on both Gram-negative and positive bacteria, depending on the concentration of the dopant and the type of microorganism, with ZM 1 % being the most effective. A smaller amount of dopant (ZM 1 %) was more effective in generating a greater antimicrobial effect, because the replacement of Zn^{2+} ions by Mg^{2+} ions allowed a change in the conformation of the nanoparticle without losing the characteristic structure of the majority salt.

Mixed oxides may act by two mechanisms, the first by allowing excessive formation of reactive oxygen species (ROS), which lead to oxidative stress and ultimately to cellular damage. Another possibility lies within the nanometric size that this material exhibits, since it allows a greater proportion of atoms or molecules which are displayed on the surface instead of inside the material, causing damage to the cell membrane, by binding these to the cell membrane, finally causing leakage of intracellular contents.

References

1. Fadl, F. I. A.; Hegazy, D. E.; Maziad, N. A.; Ghobashy, M. M. *Int. J. Biol. Macromol.* **2023**, 250, 126248.
2. Gnanam, S.; Shynu, R. K.; Gajendiran, J.; Karthikeyan, M.; Ramana Ramya, J.; Thennarasu, G. *Chem. Phys. Lett.* **2024**, 857, 141702.
3. Nigam, A.; Saini, S.; Rai, A. K.; Pawar, S. J. *Ceram. Int.* **2021**, 47, 19515–19525.
4. Halfadji, A.; Bennabi, L.; Giannakis, S.; Marrani, A. G.; Bellucci, S. *Ceram. Int.* **2024**, 50, 39097–39108.
5. Elbasuney, S.; El-Sayyad, G. S.; Tantawy, H.; Hashem, A. H. *RSC Adv.* **2021**, 11, 25961–25975.
6. Jin, S. E.; Jin, H. E. *Nanomaterials.* **2021**, 11, 263.
7. Kumar, P.; Saravanan, P.; Baskar, G.; Chitrashalini, S.; Omer, S. N.; Subashini, S.; et al. *Inorg. Chem. Commun.* **2024**, 170, 113443.
8. Garza-Cervantes, J. A.; Escárcega-González, C. E.; Díaz Barriga Castro, E.; Mendiola-Garza, G.; Marichal-Cancino, B. A.; López-Vázquez, M. A.; et al. *Int. J. Nanomedicine.* **2019**, 14, 2557–2571.
9. EL-Moslami, S. H. *Sci. Rep.* **2018**, 8, 3820.
10. Yang, X.; Wang, D.; Zhou, Q.; Nie, F.; Du, H.; Pang, X.; et al. *BMC Microbiol.* **2019**, 19, 240.
11. Bondarenko, O.; Juganson, K.; Ivask, A.; Kasemets, K.; Mortimer, M.; Kahru, A. *Arch. Toxicol.* **2013**, 87, 1181–1200.
12. Champagne, C.P.; Ross, R. P.; Saarela, M.; Hansen, K. F.; Charalampopoulos, D. *Int. J. Food Microbiol.* **2011**, 149, 185–193.
13. Christobel, G. J. *Int. J. Sci. Res.* **2013**, 5, No. NOV164755.
14. CH, A.; Rao, K. V.; Chakra, CH. S. *J. Nanomed. Nanotechnol.* **2015**, 6, 06.
15. Kayani, Z. N.; Iqbal, M.; Riaz, S.; Zia, R.; Naseem, S. *Mater. Sci.-Pol.* **2015**, 33, 515–520.
16. Rouchdi, M.; Salmani, E.; Fares, B.; Hassanain, N.; Mzerd, A. *Results Phys.* **2017**, 7, 620–627.
17. Yousefi, R.; Zak, A. K.; Jamali-Sheini, F. *Mater. Sci. Semicond. Process.* **2013**, 16*, 771–777.
18. Dobrucka, R. *Int. J. Environ. Anal. Chem.* **2021**, 101, 2046–2057.
19. Kumar, A.; Pandey, A. K.; Shanker, R.; Dhawan, A. *Microorganisms* **2012**.
20. Al-Bedairy, M.; Alshamsi, H. A. H. *Eurasian J. Anal. Chem.* **2018**, 13, No. 6.
21. Shi, X. H.; Ban, J. J.; Zhang, L.; Sun, Z. P.; Jia, D. Z.; Xu, G. C. *RSC Adv.* **2017**, 7, 16189–16195.
22. Zaidi, B.; Belghit, S.; Ullah, M. S.; Hadjoudja, B.; Guerraoui, A.; Gagui, S.; et al. *Metallofiz. Noveishie Tekhnol.* **2019**, 41, 1121–1126.
23. Kumar, R.; Sharma, A.; Kishore, N. *Int. J. Eng. Appl. Manag. Sci. Paradigms* **2013**, 07.
24. Sankara Reddy, B.; Venkatramana Reddy, S.; Koteeswara Reddy, N. *J. Mater. Sci.: Mater. Electron.* **2013**, 24, 5204–5210.

25. Auger, S.; Henry, C.; Péchaux, C.; Lejal, N.; Zanet, V.; Nikolic, M. V.; et al. *Ecotoxicol. Environ. Saf.* **2019**, 182, 109421.
26. Guan, G.; Zhang, L.; Zhu, J.; Wu, H.; Li, W.; Sun, Q. *J. Hazard. Mater.* **2021**, 402, 123542.